Supplementary Information:

An Atomically Tailored Chiral Magnet for Small Skyrmions at Room Temperature

Tao Liu[1*], Camelia M. Selcu[1*], Binbin Wang[2,3], Núria Bagués[2,3], Po-Kuan Wu[1], Timothy Q. Hartnett[4], Shuyu Cheng[1], Denis Pelekhov[1], Roland A. Bennett[1], Joseph Perry Corbett[1], Jacob R. Repicky[1], Brendan McCullian[1], P. Chris Hammel[1], Jay A. Gupta[1], Mohit Randeria[1], Prasanna V. Balachandran[4,5], David W. McComb[2,3], Roland K. Kawakami[1†]

[1]Department of Physics, The Ohio State University, Columbus, Ohio 43210, USA
[2]Center for Electron Microscopy and Analysis, The Ohio State University, Columbus, Ohio 43212, USA
[3]Department of Materials Science and Engineering, The Ohio State University, OH 43210, USA
[4]Department of Materials Science and Engineering, University of Virginia, Charlottesville, VA 22902, USA
[5]Department of Mechanical and Aerospace Engineering, University of Virginia, Charlottesville, VA 22902

*These authors contributed equally to this work
†Corresponding author. E-mail: kawakami.15@osu.edu

Contents

1. Density Functional Theory Calculations of Fe-rich FeGe

Overview

A series of density functional theory (DFT) calculations present a consistent picture indicating the preferential occupation of excess Fe atoms in the sparse layers of the B20 crystal. These calculations do not attempt to model the complex growth kinetics and do not consider interfaces with substrates. Instead, the DFT calculations are bulk-like with unit cells and periodic boundary conditions. To connect the bulk-like calculations to (111) films, the in-plane lattice parameters within the (111) planes are held fixed while the out-of-plane lattice parameter between the (111) planes is allowed to relax. The energetics of Fe incorporation are investigated by adding excess Fe atoms and allowing the system to converge to a minimum energy configuration. While this does not model the complexities of real thin film systems, it nevertheless illustrates the preferential incorporation of excess Fe into the sparse layers, consistent with the experimental protocol for atomic layer MBE.

Supercells of (111)-oriented FeGe

The unit cell of a bulk FeGe contains eight atoms (4 Fe and 4 Ge). All Fe- and Ge-atoms share a unique Wyckoff site each. All DFT calculations were performed using a (111)-oriented FeGe supercell that contained 24 atoms (12 Fe and 12 Ge). See Methods section in the main manuscript for additional information. The DFT optimized in-plane and out-of-plane lattice constants for the stoichiometric (111)-FeGe are 6.5053 and 7.9673 Å, respectively. The crystal structure is shown in **Figure S1**. The dense and sparse atomic arrangements of Fe atoms in the structure are also labeled in **Figure S1**. This specific supercell configuration support three dense and sparse layers of Fe atoms. We used this stoichiometric atomic arrangement as a baseline, and systematically introduced excess Fe atoms into the structure to understand its preferential occupation in the interstitial sites. We investigated three additional non-stoichiometric compositions using DFT calculations: $Fe_{1.08}Ge$ (with 1 excess Fe atom), $Fe_{1.17}Ge$ (with 2 excess Fe atoms), and $Fe_{1.25}Ge$ (with 3 excess Fe atoms).

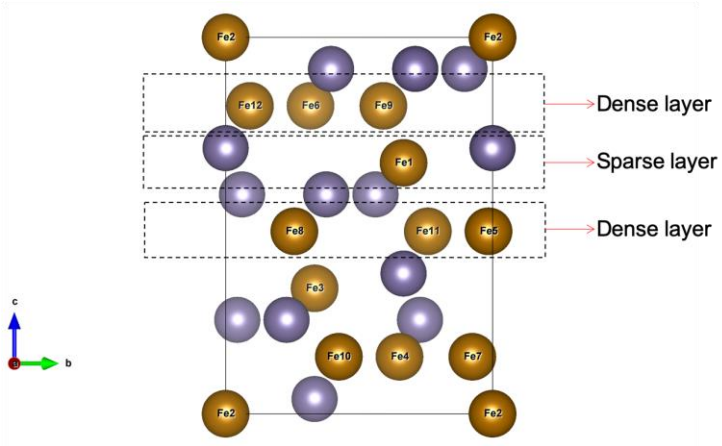

Figure S1. Crystal structure of a bulk (111)-oriented stoichiometric FeGe. The dense and sparse arrangements of Fe atoms are labeled. The brown and purple atoms correspond to Fe and Ge, respectively.

$Fe_{1.08}Ge$ with one excess Fe atom:

Our first set of calculations involved introducing one excess Fe atom in the dense and sparse layers. In our calculations, the in-plane lattice constants were fixed, whereas the out-of-plane lattice constants were allowed to relax. All internal coordinates were allowed to relax. The fully relaxed crystal structures are shown in **Figure S2**. We were able to identify a local minimum for the excess Fe atom in both the structures (labeled as "Fe13" in **Figure S2**). In **Figure S2a**, the excess Fe atom occupies the dense layer and in **Figure S2b**, it occupies the sparse layer. Further, the crystal structure shown in **Figure S2b,** where we have an excess Fe atom in the sparse layer, was 20 meV/atom *lower* in total energy compared to the structure shown in **Figure S2a**. This initial result indicated the preferential occupation of the excess Fe atom in the sparse layers of the (111)-oriented FeGe structure. The out-of-plane lattice constant increased to 8.2636 Å for the lowest energy structure (**Figure S2b**).

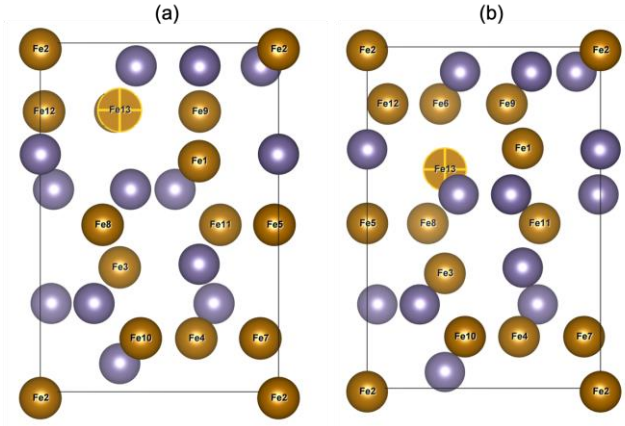

Figure S2. Crystal structures of fully relaxed $Fe_{1.08}Ge$ composition with one excess Fe atom (labeled as "Fe13") in the (a) Dense and (b) Sparse layers.

$Fe_{1.17}Ge$ with two excess Fe atoms:

Our second set of calculations involved introducing two excess Fe atoms into the structure. The composition of the new structure corresponds to $Fe_{1.17}Ge$, which is closer to that of the experimental $Fe_{1.2}Ge$ composition. Informed by the first set of results from DFT, we introduced the two excess Fe atoms into the sparse layers. Our choice of the (111)-FeGe supercell permitted three different locations for the distribution of the excess two Fe atoms in the three sparse layers. We explored all three locations. Similar to the previous calculation, the in-plane lattice constants were fixed and the out-of-plane lattice constants were allowed to relax. All internal coordinates were also allowed to relax. The results from the converged DFT calculations are shown in **Figure S3**. All three configurations have unique local minima and the excess Fe atoms occupy the sparse layers. Intriguingly, the excess Fe atoms form their own *new* sparse layers in the structure. All three structures were practically degenerate (the energy difference was of the order of 0.01 meV/atom). The out-of-plane lattice constant increased to 8.903-8.904 Å.

In addition to the configurations shown in **Figure S3**, we also tested another atomic arrangement. In this case, we initialized the two excess Fe atoms in the dense layers and let all atoms to relax to equilibrium positions. The out-of-plane lattice constant was also allowed to relax. The initial and fully relax crystal structures are shown in **Figure S4a** and **Figure S4b**, respectively. The DFT calculations were initialized with both excess Fe atoms co-planar in the dense layer (the *z*-coordinate of the excess and native Fe atoms in the dense layers are shown in **Figure S4a)**. In the relaxed configuration, there were two interesting outcomes. First, the excess atom Fe13

diffused out of the dense layer and formed its own sparse layer. This atomic arrangement is consistent with the expected trend seen in **Figures S2** and S**3**. Second, the excess atom Fe14 remained in close proximity to the initial position in the dense layer, but disrupted the symmetry and coplanarity of the initial dense Fe layers. The *z*-coordinate of the relaxed configuration is labeled in **Figure S4b** to accentuate this finding. The three unique Fe atoms in the dense layers have three unique *z*-coordinate, which is indicative of the lack of co-planar arrangement. The co-planar arrangement of the dense layers is an important fingerprint of the high-symmetry B20 materials class (see **Figure S1**). Intriguingly, this atomic arrangement also has a profound impact on the sparse and dense Ge layers. The Ge atoms also lose the coplanar atomic arrangement due to this configuration. It is important to note that such a disruption is not observed in **Figure S3**.

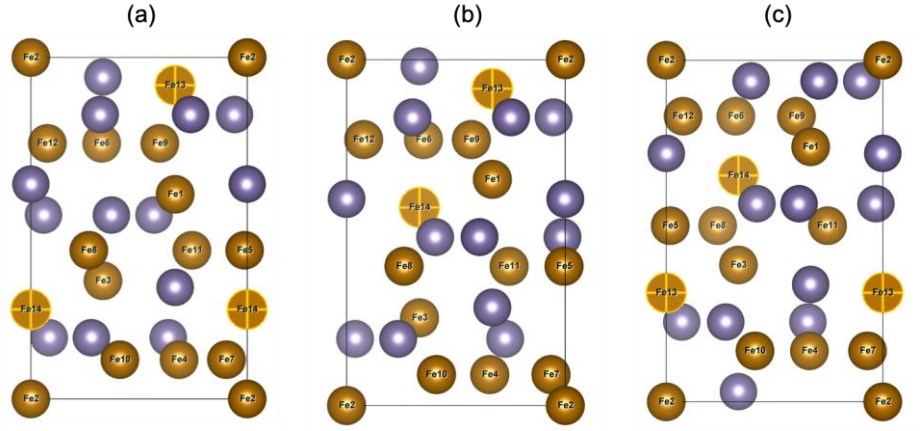

Figure S3. Crystal structures of fully relaxed $Fe_{1.17}Ge$ composition with two excess Fe atoms in the sparse layers (labeled as "Fe13" and "Fe14"). All excess Fe atoms form their own "new" sparse layers in the structure.

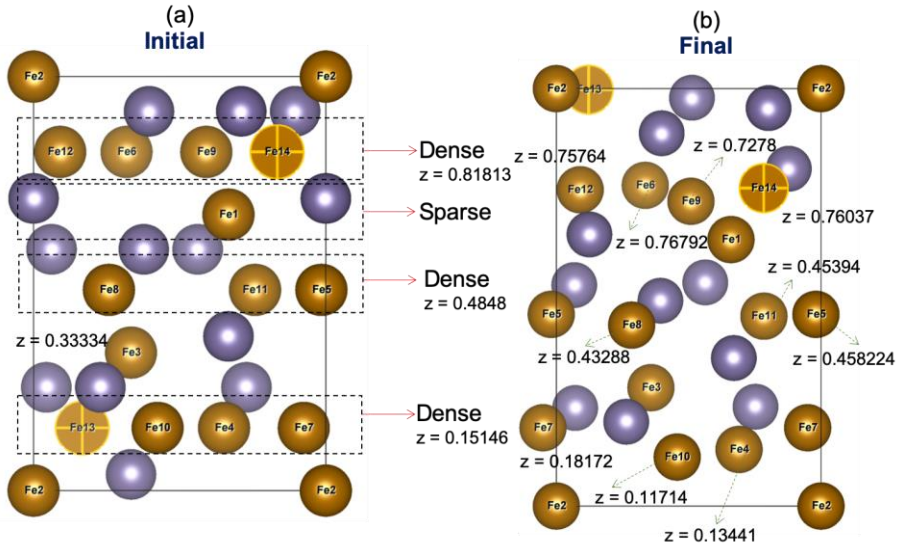

Figure S4. Crystal structures of (a) an initial and (b) fully relaxed $Fe_{1.17}Ge$ composition with two excess Fe atoms (labeled as "Fe13" and "Fe14"). In (a) both excess Fe atoms are in the dense layers. In (b) atom Fe13 is on the sparse layer and atom Fe14 disrupts the symmetry of the dense layer and is no longer coplanar with the initial dense layer.

We identify the structures shown in **Figure S3** to have a higher symmetry than that shown in **Figure S4b**. The relaxed final structure in **Figure S4b** has an out-of-plane lattice constant value of 8.8895 Å. However, the structure shown in **Figure S4b** is 58.4 meV/atom *lower* in energy compared to that shown in **Figure S3**. Our DFT calculations suggest that the lowest energy configuration for the $Fe_{1.17}Ge$ composition has a lower symmetry.

$Fe_{1.25}Ge$ with three excess Fe atoms:

Finally, we also explored another atomic configuration with three excess Fe atoms in the sparse layers. In this simulation, we relaxed all internal coordinates and the out-of-plane lattice constant. The fully relaxed structure is shown in **Figure S5**, where the excess Fe atoms are labeled as "Fe13", "Fe14" and "Fe15". All excess Fe atoms occupy the sparse layers in the structure. Similar to the structures shown in **Figure S3**, the excess Fe atoms form their own *new* sparse layers in the crystal structure. Further, the coplanarity of the dense Fe and Ge layers are also maintained in this atomic arrangement (indicative of a crystal structure with higher symmetry). The calculated out-of-plane lattice constant is 9.5369 Å.

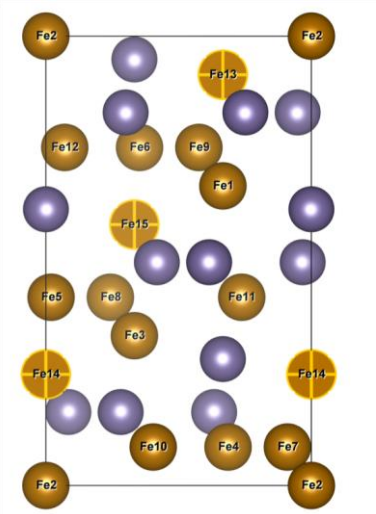

Figure S5. Crystal structure of a fully relaxed $Fe_{1.25}Ge$ composition with three excess Fe atoms (labeled as "Fe13", "Fe14", and "Fe15") in the sparse layers.

One of the main findings from the DFT calculations is that when the excess Fe atoms are located in the sparse layers, we get a high symmetry structure that is similar to those seen in the experimentally grown thin films. Although there are lower energy structures, these atomic arrangements occur at the expense of the crystal symmetry. Since the X-ray diffraction data and transmission electron micrograph on the experimentally grown thin films showed strong evidence for a high symmetry B20-like crystal structure, we conclude that the structures shown in **Figure S3**, where the excess Fe atoms occupy the sparse layers, are more representative of the symmetry of our thin films.

Supercells of bulk FeGe simulations

In addition to the (111)-oriented FeGe crystal structures, we also performed DFT calculations on the bulk FeGe. We created a 2x2x1 supercell with 32 atoms (16 Fe and 16 Ge atoms). The crystal structure is shown in **Figure S6**.

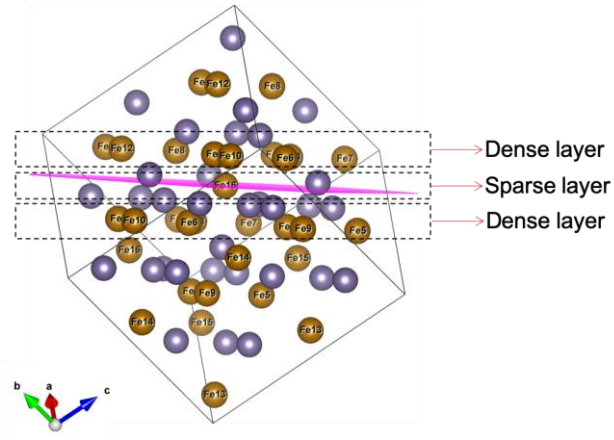

Figure S6. Crystal structure of bulk, stoichiometric FeGe. The crystal structure is rotated to highlight the atomic arrangements in dense and sparse layers. The magenta color plane is drawn as a guide to the eye, which intersects atom Fe16 on the sparse layer. Fe- and Ge-atoms are shown in brown and purple colors, respectively.

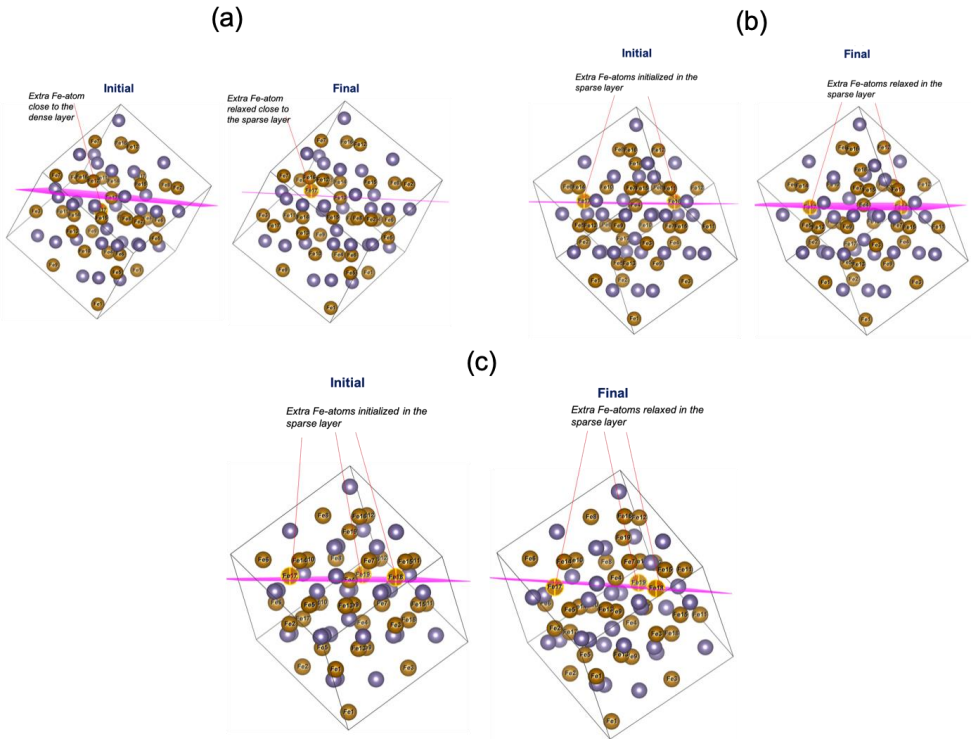

Figure S7. Crystal structures of bulk, FeGe supercells with (a) one excess Fe atom ("Fe17"), (b) two excess Fe atoms ("Fe18" and "Fe19"), and (c) three excess Fe atoms ("Fe17", "Fe18" and "Fe19").

We then systematically added one, two, and three excess Fe atoms into the structure and allowed the internal coordinates and out-of-plane lattice constant to relax. The results are shown in **Figure S7**. In **Figure S7a**, we initialized the structure with the excess Fe atom ("Fe17") in the dense layer. However, the Fe17 atom diffused out of the dense layer and relaxed in the near-by sparse layer. In **Figures S7b** and S**7c**, we show the results for the two and three excess Fe atoms, respectively. In both cases, we initialized the DFT calculations with the excess Fe atoms in the sparse layer. The calculations converged with those excess Fe atoms relaxing in the sparse layer. All DFT results paint a consistent picture indicating the preferential occupation of excess Fe atoms in the sparse layers of the B20 crystal structure.

2. MFM images without circles

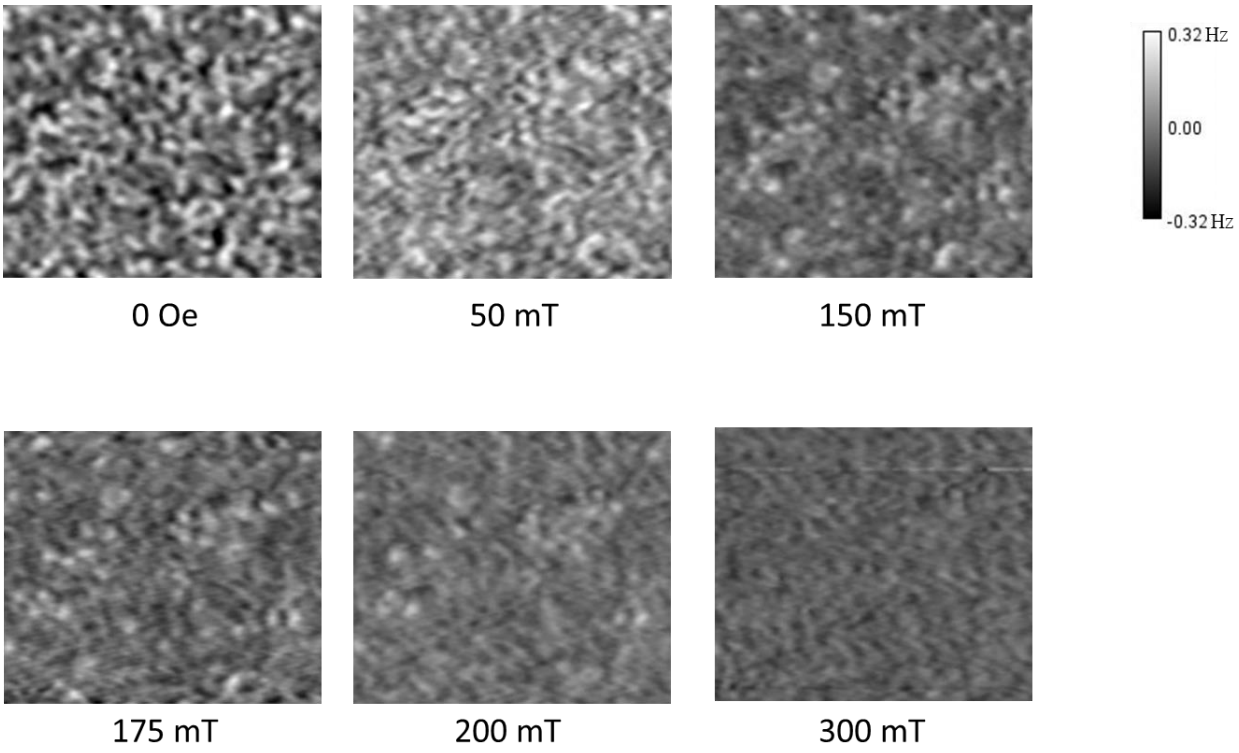

Figure S8. MFM images of Figure 3 of the main text without circling the skyrmions.

3. Topological Hall Effect Measurements and Analysis

The total Hall resistivity, ρ_{xy}, is the sum of three contributions: (1) the ordinary Hall effect ρ_{OH}, a result of the Lorentz force, that is proportional to the magnetic field strength (H); (2) the anomalous Hall effect ρ_{AH}, which is proportional to z-component of magnetization (M_z); and (3) the topological Hall effect ρ_{TH}, resulting from the reflecting of electrons or holes by real space topological spin textures, i.e.,

$$\rho_{xy} = \rho_{OH} + \rho_{AH} + \rho_{TH} = R_0 H + R_{AH} M + \rho_{TH} \quad (1)$$

where R_0 and R_{AH} are the ordinary Hall coefficient and anomalous Hall coefficient, respectively. Dividing both sides of equation (1) by H,

$$\rho_{xy}/H = R_0 + R_{AH}\, M/H + \rho_{TH}/H \quad (2)$$

In the high field range, where magnetizations have been totally saturated and the topological spin textures have been eliminated, the $\rho_{AHE} = 0$, then equation (2) can be simplified to

$$\rho_{xy}/H = R_0 + R_{AH}\, M/H \quad (3)$$

Therefore, we measure both the ρ_{xy} vs. H and M vs. H on the same sample. Plotting ρ_{xy}/H vs. M/H at the range of H that is larger than the saturation field and doing linear fit, then we could obtain the R_0 and R_{AH} from the y-intercept and the slope of the fitting line. Consequently, we could separate the three contributions from Hall resistivity.

Based on the above analysis, we obtained the phase diagraph of ρ_{THE} of our Fe-rich $Fe_{1.2}Ge$ using the following procedure:

(1) Measure both the ρ_{xy} vs. H and M vs. H of a Fe-rich $Fe_{1.2}Ge$ sample. These start at +7 Tesla and ramp down to -7 Tesla and is denoted as $\rho_{xy}^{-}(H)$, followed by a scan from -7 Tesla to +7 Tesla and is denoted as $\rho_{xy}^{+}(H)$. Considering the Hall resistivity should be antisymmetric in H, we remove any longitudinal resistance leaking into the transverse signal (which is symmetric in H) by anti-symmetrizing the resistivity data according to $\tilde{\rho}_{xy}^{+}(H) = \frac{1}{2}\left[\rho_{xy}^{+}(H) - \rho_{xy}^{-}(-H)\right]$ and $\tilde{\rho}_{xy}^{-}(H) = \frac{1}{2}\left[\rho_{xy}^{-}(H) - \rho_{xy}^{+}(-H)\right]$.

(2) Plot $\tilde{\rho}_{xy}^{+}/H$ vs. M/H at the range of $H > 2$ T (in saturation).

(3) Linearly fit $\tilde{\rho}_{xy}^{+}/H$ vs. M/H to obtain R_0 and R_{AH} from the y-intercept and the slope.

(4) Calculate $\rho_{OH} = R_0 H$ and $\rho_{OH} = R_{AH} M$

(5) Calculate $\rho_{TH} = \tilde{\rho}_{xy}^{+} - \rho_{OH} - \rho_{AH}$ (and $\rho_{TH} = \tilde{\rho}_{xy}^{-} - \rho_{OH} - \rho_{AH}$)

(6) Repeat steps (1)-(5) at different temperatures, we obtain the ρ_{TH} at different temperatures to obtain a phase diagram. By convention, we plot $\rho_{TH} = \tilde{\rho}_{xy}^{+} - \rho_{OH} - \rho_{AH}$ vs. T and H for the phase diagram.

Figures S9 and S10 show a representative set of Hall resistivity data analysis results which obtain at a temperature of 340 K. As one can note that a clear topological Hall resistance component, with unique antisymmetric shape similar to that of previous reported ordinary FeGe

films,[1] has been obtained even at a temperature much higher than the Curie temperature of ordinary FeGe.

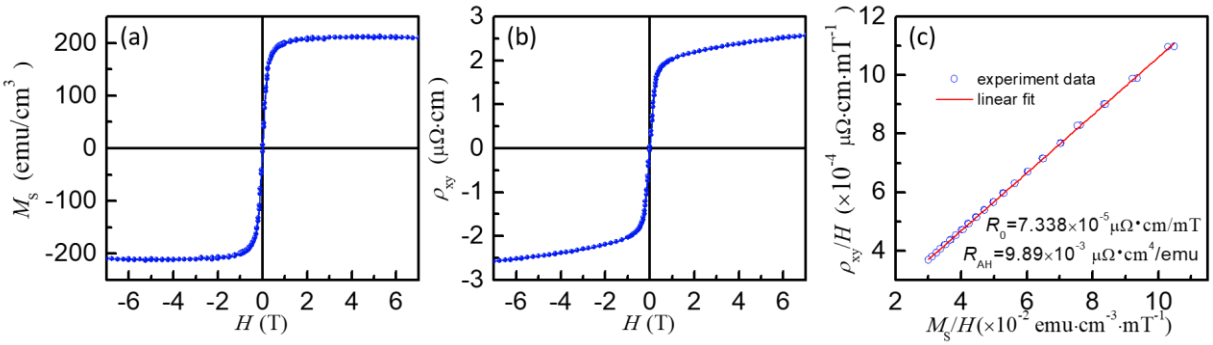

Figure S9. (a) Hysteresis loop and (b) Hall resistivity of a Fe-rich $Fe_{1.2}Ge$ sample, both of which are measured at 340 K in a Quantum Design PPMS using exactly the same field scanning procedure. (c) Linear fit of the ρ_{xy}/H vs. M/H at $H > 2$ T. The ρ_{xy} have been anti-symmetrized.

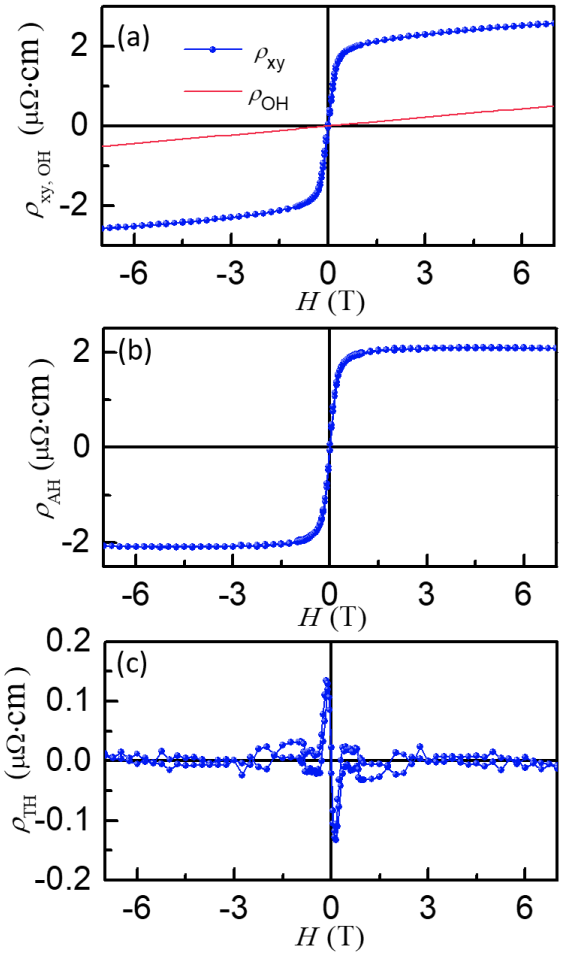

Figure S10. (a) ρ_{xy} and ρ_{OH}, (b) ρ_{AH}, and (c) ρ_{TH} of the Fe-rich $Fe_{1.2}Ge$ sample at 340 K, obtained using our Hall resistivity analysis method. The ρ_{xy} have been anti-symmetrized (i.e. $\tilde{\rho}_{xy}^{+}$ and $\tilde{\rho}_{xy}^{-}$)

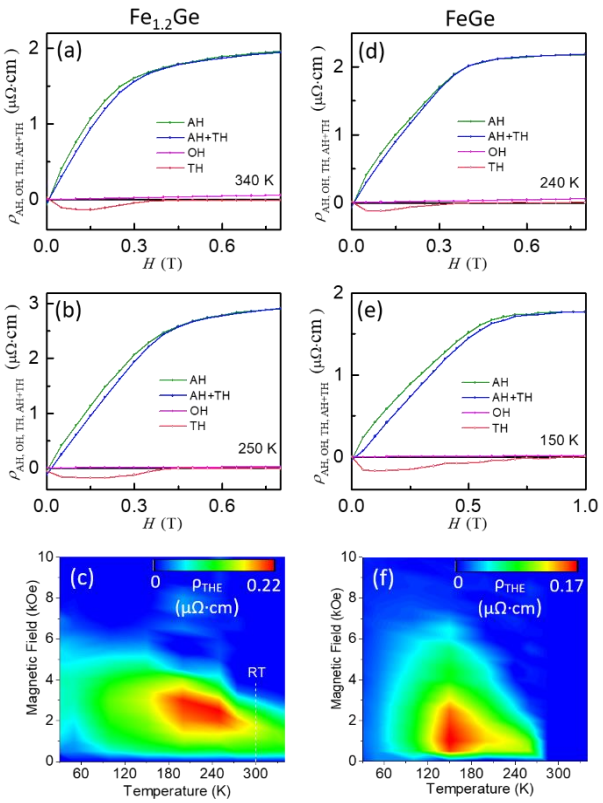

Figure S11. Comparing the topological resistivity of Fe-rich $Fe_{1.2}Ge$ and ordinary FeGe. The fourth quarter part of ρ_{AH} , $\rho_{AH}+\rho_{TH}$ and ρ_{TH}, which have the same magnetic field scanning procedure as that for taking MFM images, of (a)(b) $Fe_{1.2}Ge$, and (d)(e) FeGe at several representative temperatures. ρ_{TH} vs. field and temperature phase diagraph of (c) $Fe_{1.2}Ge$ and (f) FeGe.

Note that the relative values of ρ_{TH} to that of ρ_{xy} and ρ_{AH} are always very small. Therefore, the hysteresis loop and Hall resistivity measurements and data analysis procedures need to be carried out very carefully. To minimize the contamination of ρ_{TH} by any artificial effect, the following schemes had been taken: (1) In previously reported topological Hall resistivity measurements,[1] the hysteresis loops and Hall resistivity loops were always measured using two facilities. For example, the hysteresis loops were measured by SQUID and the Hall resistivity loops were measured by PPMS. To make sure the magnetic fields in corresponding magnetic and transport data are exactly the same, both measurements were both performed in the same Quantum Design PPMS system and the employed field scan procedures were identical. (2) The longitudinal resistivity was also measured during the Hall resistivity measurements, so that the longitudinal resistivity mixed into Hall resistivity due to device asymmetry can be well subtracted. We found that the most reliable method for removing the longitudinal resistivity is the anti-symmetrization procedure discussed earlier.

In order to validate of our approach for obtaining ρ_{TH}, we have also fabricated an ordinary FeGe film, in which we had observed skyrmions with size similar to previous reports using L-TEM.[2,3] The obtained topological resistivity of Fe-rich $Fe_{1.2}Ge$ and ordinary FeGe films are presented in **Figure S11**.

4. Comparison of Topological Hall Effect and MFM Measurements as a Function of Applied Field

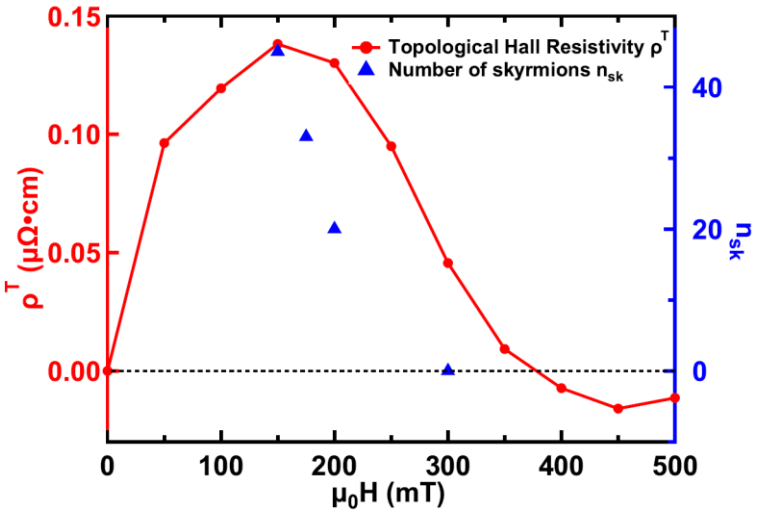

Figure S12. Comparing the topological Hall resistivity of Fe-rich $Fe_{1.2}Ge$ at room temperature (red curve) with the skyrmion density as determined by MFM. The former is a linecut from the data in Figure 3g (replotted in Figure S11c) and the latter is determined from the skyrmions identified in Figures 3c-3f of the main text.

Theoretically, the topological Hall effect is proportional to the skyrmion density, but experimentally, the relationship between the two quantities is less well established. In this section, we consider the magnetic field dependence of the two quantities and in the next section, we estimate the magnitude of the topological Hall resistivity (THR) based on a Drude model-like analysis.

For the skyrmions observed at room temperature, the experimental field dependence of the skyrmion density measured by MFM and the topological Hall resistivity are shown in **Figure S12**. We observe some similar qualitative trends. The skyrmion density is high at 150 mT, which is where the magnitude of the THR is maximized. With increasing magnetic field, both the skyrmion density and the THR decrease in magnitude, eventually reaching zero at high magnetic fields.

However, there is not a quantitative agreement between the skyrmion density and the THR. Specifically, the THR is not observed to be proportional to the skyrmion density. The skyrmion density is observed to decrease more rapidly than the THR with increasing field, and the skyrmion density reaches zero by 300 mT where THR is still observed. At least two possible effects could play a role in this discrepancy. First, magnetic features unrelated to skyrmions could produce contributions to the Hall resistivity that are not simply proportional to the magnetization, thus contributing to the extracted topological Hall signal following the procedure described in section 3 (see for example, references 4 and 5). Second, the presence of magnetic field generated by the tip could shift the data for skyrmion density vs. field. With an estimated tip field of ~ 25 mT, this should shift the skyrmion density data point to the right, or higher field, by ~25 mT. This could reduce the discrepancy but not explain it completely.

5. Topological Hall Resistivity (THR) Estimates

We use the Drude model-like analysis of P. Bruno *et al.*[6] to make a simple estimate of the topological Hall effect. We could use Eqs. (13,14) of N. Verma *et al.*[7] for an arbitrary band structure, but our goal here is just an order-of-magnitude estimate.

We make a further simplification by letting the scattering time t_s = t independent of the spin label s. Then eq. (6) and (7) of Bruno PRL lead to a THR result which can be written as

$$\rho_{xy} = P\, R_H\, B_{eff}$$

where R_H = 1/ne is the usual Hall coefficient, $B_{eff} = n_{sk}$ (h/e) = (skyrmion density x flux quantum) is the "effective magnetic field", and P = $(n_u - n_d)/(n_u + n_d)$ is conduction electron polarization with u = up and d = down. Going beyond a Drude-like theory, P will actually involve the conduction electron DOS at the Fermi surface, i.e., n_u will be replaced by $N_u(0)$ and n_d by $N_d(0)$; but this will not affect the simple estimates. P should lie between 0 and 1, and for now we will just treat it as an unknown of order 1.

Using the measured R_H in the ordinary Hall regime at high fields, and h/e = 4.14 x 10^{-15} Tm^2, we get the following results

	FeGe (200 K, 200 mT)	Fe-rich FeGe (300 K, 150 mT)
Measured R_H (μΩ cm/T)	0.39	0.61
Measured n_{sk} (m^{-2})	60.7 x 10^{12}	15.6 x 10^{12}
Estimated B_{eff} (T)	0.25	0.065
Estimated topo ρ_{xy} (μΩ cm)	0.098	0.039
Measured topo ρ_{xy} (μΩ cm)	0.1528	0.1548

We see that this simple theory is off by a factor of 2-4 from the THR Data. We assumed P = 1 so, if P is actually 0.1 we are further off by a factor of 10. The sign is not issue since P can be either positive or negative.

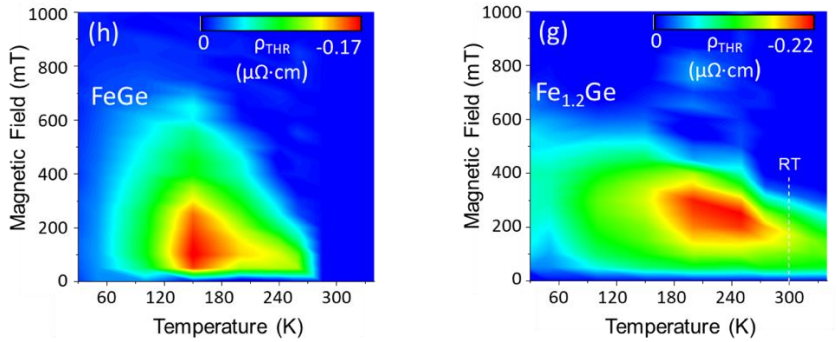

Figure S13. Plots of topological Hall resistivity as a function of magnetic field and temperature for an epitaxial FeGe film (left) and Fe-rich FeGe film (right).

6. Determination of Micromagnetic Parameters

We discuss the determination of the micromagnetic parameters: saturation magnetization M_s, exchange stiffness A_{ex}, bulk Dzyaloshinskii-Moriya interaction (DMI) D, magnetic anisotropy K_u, and the Gilbert damping α. These parameters are a succinct way to describe the magnetism in a material via the effective free energy function

$$\mathcal{F} = A_{ex}(\nabla \boldsymbol{m})^2 + D\boldsymbol{m} \cdot (\nabla \times \boldsymbol{m}) - K_u m_z^2 - H m_z$$

Here $\boldsymbol{m}$ is the unit vector of magnetization ($\boldsymbol{m} = \boldsymbol{M}/M_S$), and the D term describes the bulk DMI characteristic of the non-centrosymmetric B20 crystal structure. The damping α enters the Landau Lifshitz Gilbert (LLG) equation.

One of the key questions in skyrmion materials is: what parameters determine the size and stability of skyrmions? The simplest answer is that the size of skyrmions in determined by the ratio of the exchange to DMI, namely by the length scale $L_D = 4\pi A_{ex}/D$ [8,9]. However, there are several theoretical studies, especially of isolated skyrmions, which conclude that their size is *not* determined by L_D, and that it depends in an essential way on K_u and M_s [10–12].

In view of this, it is especially important to understand the parameters that characterize small, room-temperature skyrmions in Fe-rich FeGe. We will show below, combining micromagnetic simulations with our experimental measurements (magnetization, FMR, MFM and LTEM), that the size of Bloch skyrmions is indeed determined by $L_D \sim A_{ex}/D$ and weakly dependent of K_u and M_s.

We start by summarize our results for room temperature values of the micromagnetic parameters in the table below.

M_s	253 kA/m
A_{ex}	0.69 ± 0.07 pJ/m
D	0.25 mJ/m^2
K_u	11.5 - 23 kJ/m^3
α	0.019

The saturation magnetization M_s is determined from the SQUID magnetometry measurement of *M vs. H* shown in **Figure S14** (the out-of-plane geometry is utilized to minimize effects of the point dipole approximation). We find that M_s = 253 kA/m, which is equivalent to 253 emu/cm^3.

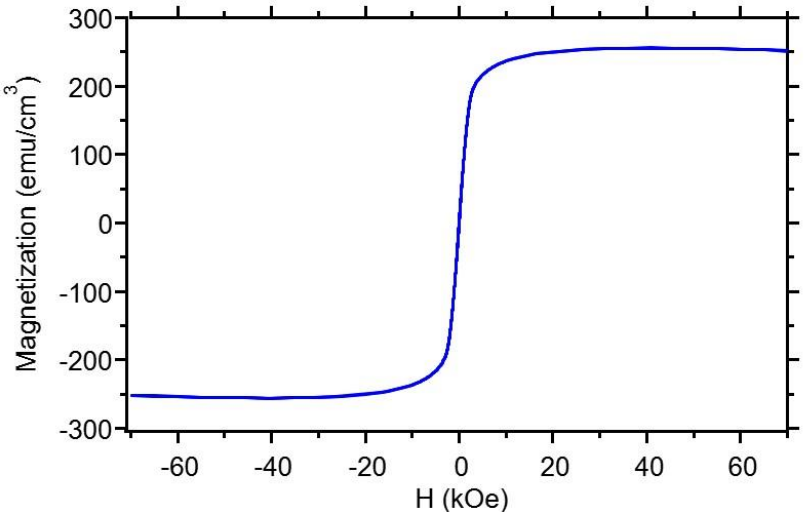

Figure S14. Out-of-plane hysteresis loop of 108 nm thick $Fe_{1.2}Ge$ film, with diamagnetic background subtracted, obtained at 300 K via SQUID magnetometry.

We use the following procedure to estimate the exchange A_{ex}. We start with the relation between the exchange stiffness and saturation magnetization at two different temperatures T_1 and T_2

$$\frac{A_{ex}(T_1)}{A_{ex}(T_2)} = \left(\frac{M_s(T_1)}{M_s(T_2)}\right)^2.$$

This can be understood by looking at how the microscopic exchange energy *J* in a spin model is related to the stiffness A_{ex} via $A_{ex} = J\, M_s^2\, a/2$, where a is the lattice spacing. The above scaling follows from the fact that the microscopic exchange *J* is a *T*-independent. Next, we use the fact that the transition temperatures T_c of two magnetic materials A and B are both proportional to their T=0 exchange stiffnesses, so that

$$\frac{A_{ex,A}(0)}{A_{ex,B}(0)} = \frac{T_{c,A}}{T_{c,B}}.$$

Combining these two equations we find

$$A_{ex,A}(T_0) = A_{ex,B}(0)\, \frac{T_{c,A}}{T_{c,B}} \left(\frac{M_{s,A}(T_0)}{M_{s,A}(0)}\right)^2.$$

We choose $T_0 = 300$ K (room temperature) for the system A of interest, namely, Fe-rich FeGe and as our reference we choose a closely related material B = $Mn_{0.08}Fe_{0.92}Ge$ for which the required data $A_{ex,\mathrm{B}}(0) = 1.47 \pm 0.14$ pJ/m and $T_{c,\mathrm{B}} = 260$ K are available from the literature[13]. From our own measurements on Fe-rich FeGe (= A) we have $M_{s,A}(300K)$ = 253 kA/m from **Figure S14** and $M_{s,A}(0)$ = 470 kA/m and $T_{c,A} = 420$ K from **Figure 2e** (main text). Using these inputs, we

find that the room temperature exchange stiffness for Fe-rich FeGe is $A_{ex,A}(300K) = 0.69 \pm 0.07$ pJ/m.

The magnetic anisotropy and damping are determined from room temperature Ferromagnetic Resonance (FMR) experiments described below. The Gilbert damping α of $Fe_{1.2}Ge$ is found to be $\alpha = 0.019$. We can constrain K_u to lie in the range 11.5 - 23 kJ/m^3 (or $1.15 \times 10^5 - 2.3 \times 10^5$ erg/cm^3). Note that the positive sign indicates an easy axis (out-of-plane) anisotropy for our Fe-rich FeGe thin films. We will show below that the uncertainty in our K_u estimates does *not* impact our micromagnetic simulations of skyrmion size and stability.

Absent a direct measurement of the Dzyaloshinskii-Moriya interaction, we use micromagnetic simulations with a single free parameter D to fit the skyrmion size, R_{sk} = 10.7 ± 4.7 nm (HWHM), measured by our LTEM and MFM experiments described in the paper. The micromagnetic results were independently checked using MuMax3[14] and our custom simulation software. We find that the skyrmion size depends crucially on DMI, and 11 nm radius skyrmions are obtained for D = 0.25 mJ/m^2 as shown in **Figure S15**. These results are only weakly dependent on the value of K_u, as seen from **Figure S16**, and also of M_s, as seen from **Figure S17**.

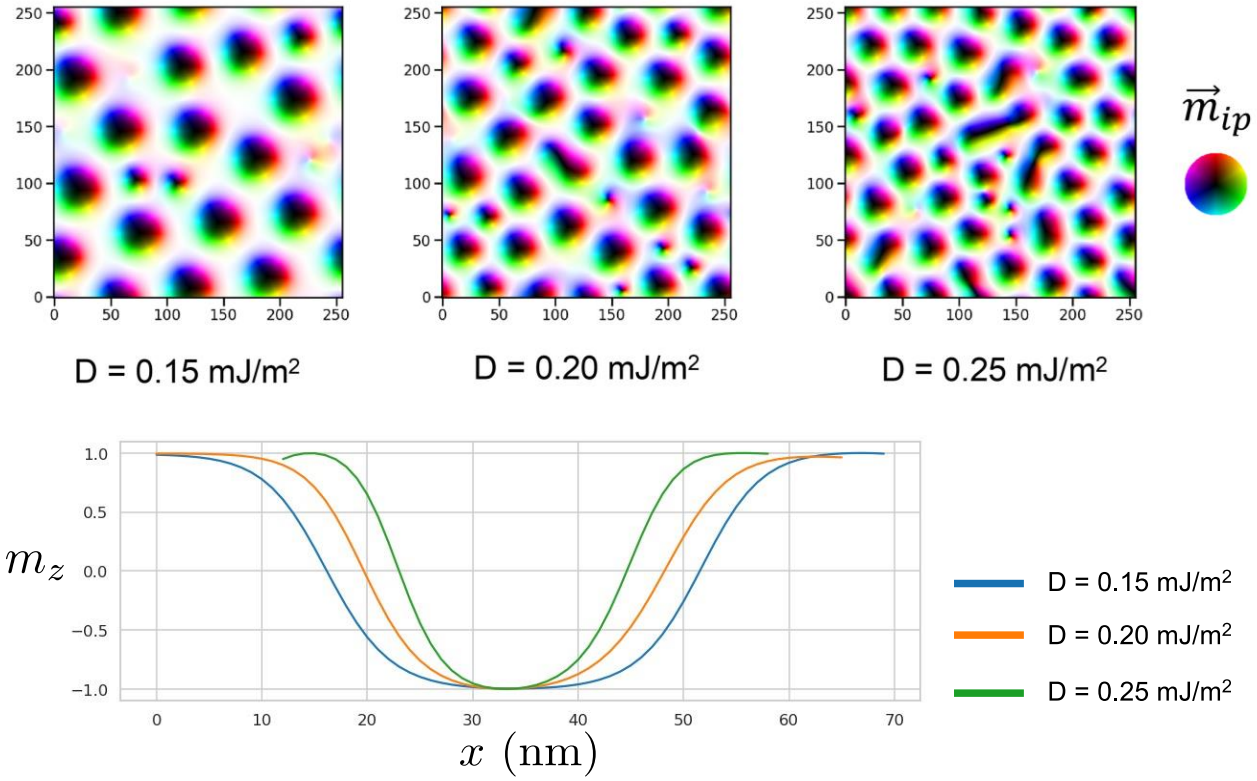

Figure S15: Results of micromagnetic simulations for skyrmion with the experimentally measured M_s = 253 kA/m, A_{ex} = 0.69 pJ/m, and K_u = 17 kJ/m^3 for a 108 nm thick film in an external field of H = 0.16 T. We show results for three different DMI values. Choosing D = 0.25 mJ/m^2 leads to skyrmions of 22 nm diameter, consistent. with our LTEM and MFM experiments. The upper panels show the in-plane (ip) magnetization, and the lower panel shows line cuts of the spatial variation of m_z, from which we define the skyrmion diameter using the zero crossings.

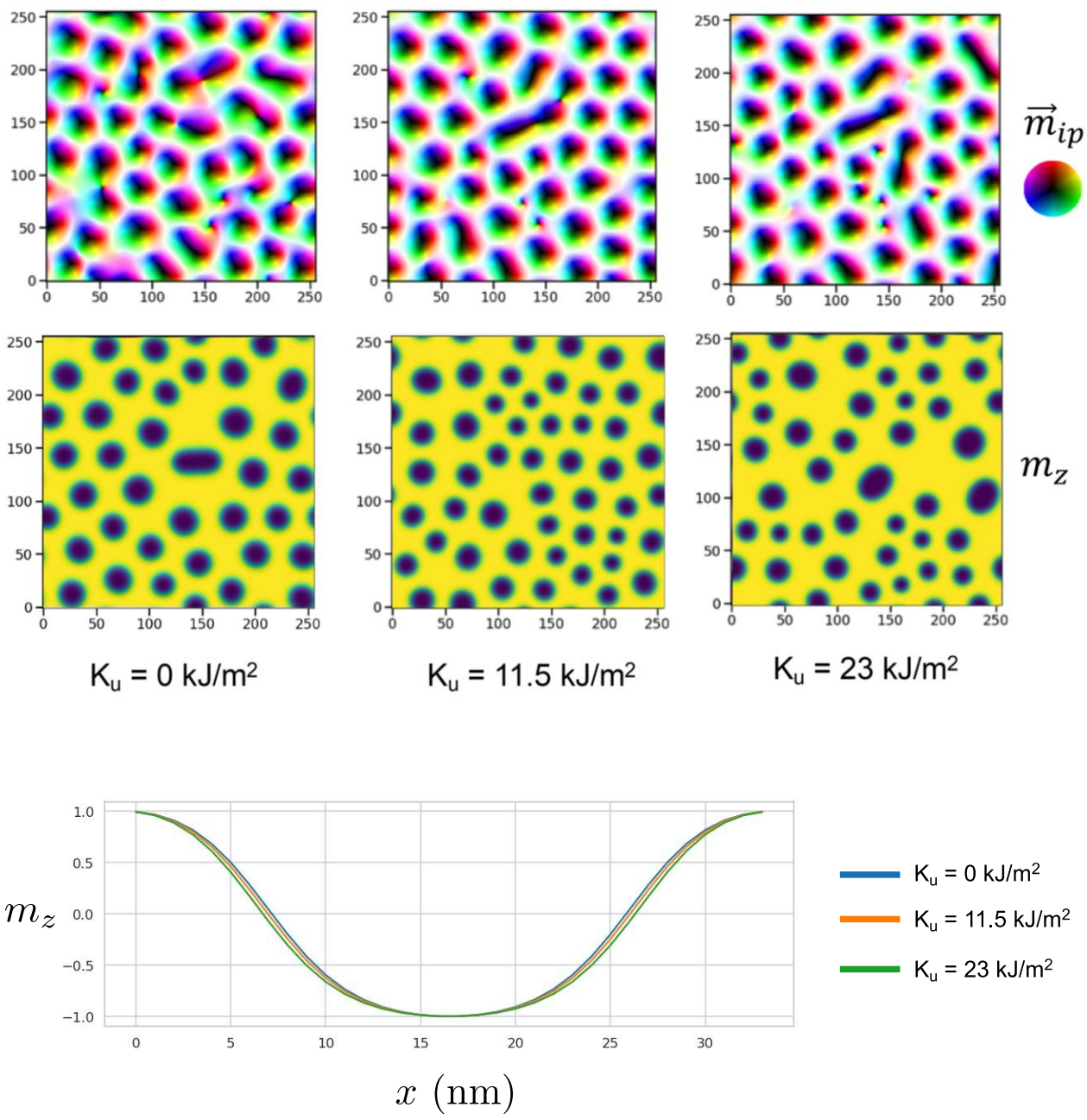

Figure S16: Results of micromagnetic simulations for skyrmion with the experimentally measured M_s = 253 kA/m, A_{ex} = 0.69 pJ/m, for a 108 nm thick film in an external field of H = 0.16 T. We chose a DMI D = 0.25 mJ/m^2 in order to get a skyrmion radius that matches our LTEM and MFM experiments. We show that the results are substantially independent of the magnetic anisotropy K_u. Note that our FMR measurements lead to K_u estimates in the range 11.5 - 23 kJ/m^3. The upper panels show the in-plane magnetization, the middle panels show m_z, while the lower panel shows line cuts of the spatial variation of m_z, from which we define the skyrmion diameter using the zero crossings.

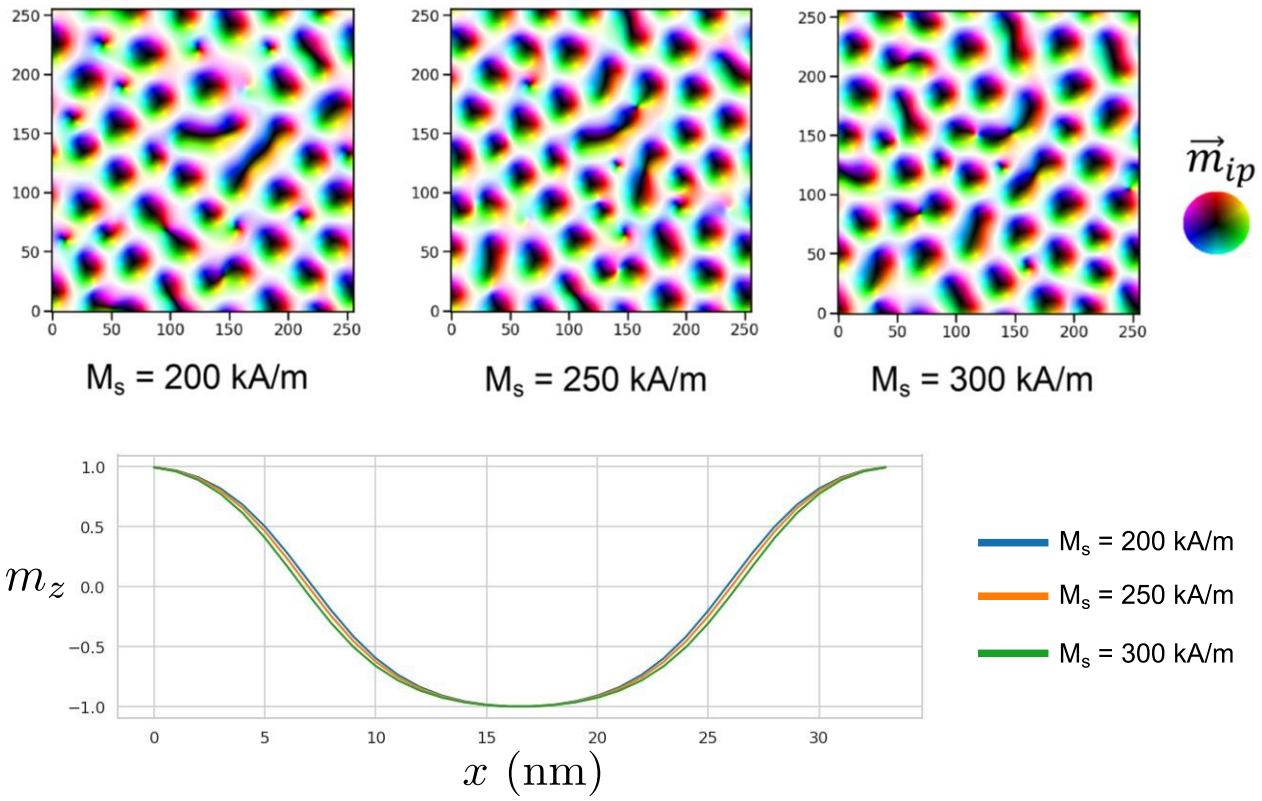

Figure S17: Results of micromagnetic simulations for skyrmion with the experimentally measured A_{ex} = 0.69 pJ/m, for a 108 nm thick film in an external field of H = 0.16 T. We chose a DMI D = 0.25 mJ/m^2 and K_u = 17 kJ/m^3. The upper panels show the in-plane magnetization, while the lower panel shows the spatial variation of m_z, from which we define the skyrmion diameter using the zero crossings. The results for skyrmion size are substantially independent over a range of M_s values around the experimentally measured M_s = 253 kA/m.

Ferromagnetic Resonance measurements

We conducted broad band Ferromagnetic Resonance (FMR) studies of 54 nm thick $Fe_{1.2}Ge$ film grown on 5 nm FeGe layer on Si substrate at room temperature and under ambient conditions. The external magnetic field was applied in the plane of the film.

Magnetic anisotropy

A series of FMR spectra, acquired via magnetic field modulation, at several frequencies of applied rf radiation is shown in **Figure S18a**. The resonant field of the signal H_{res} and the full width at half-maximum linewidth ΔH at each rf frequency was determined using Lorentzian lineshape fitting function incorporating symmetric and anti-symmetric contributions:

$$V = \frac{S + A(H - H_{res})}{((H - H_{res})^2 + (\Delta H/2)^2)^2}$$

Here V is the amplitude of the field modulated FMR signal at a given static field H, and S and A are the coefficients describing the symmetric and the anti-symmetric parts of the Lorentzian lineshape, respectively. The resulting dispersion relationship and the frequency dependence of the linewidth ΔH are shown in **Figure S18b** and **Figure S18c**, respectively.

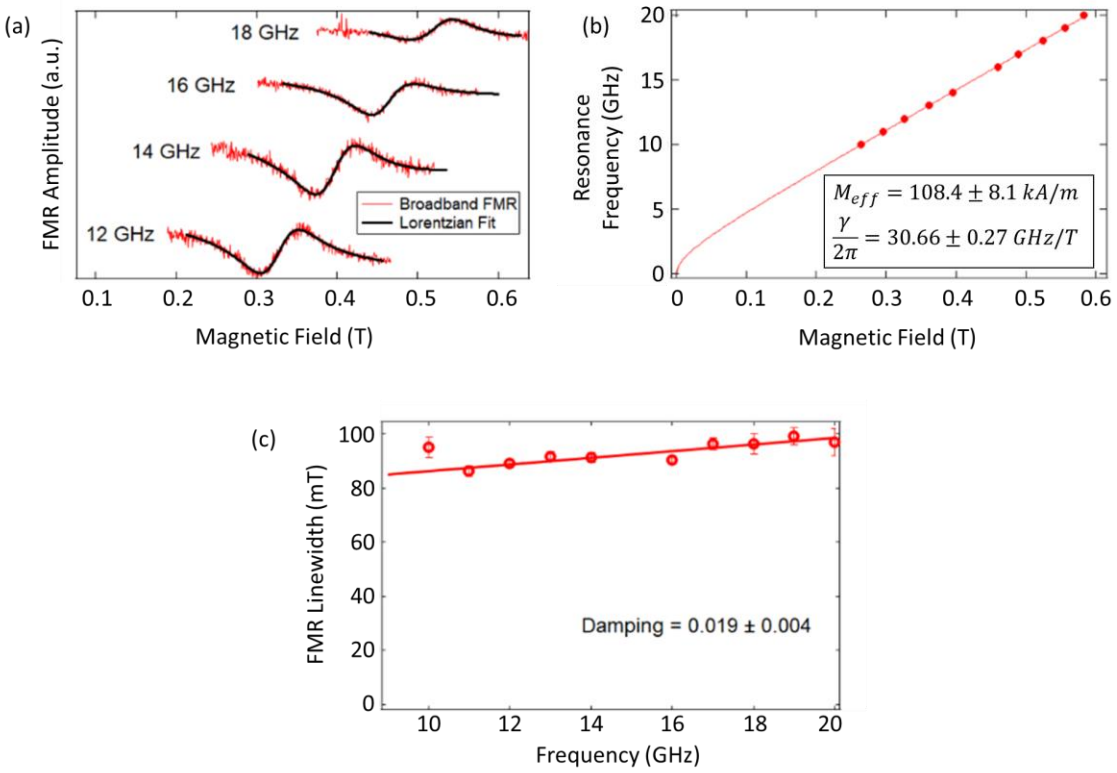

Figure S18. Room temperature broadband FMR of $Fe_{1.2}Ge$ thin film. (a) Broadband field-modulated FMR response of $Fe_{1.2}Ge$ with fits to a combined symmetric and antisymmetric Lorentzian lineshape. (b) Fit of the FMR resonance condition fit to the in-plane Kittel response for a ferromagnetic thin film. (c) Linear fit of the FMR linewidth versus frequency to extract the Gilbert damping parameter α.

We analyze the obtained dispersion relationship using the Kittel equation for the FMR resonance condition for a thin ferromagnetic film with the static field applied in the film plane:

$$f_{res} = \frac{\gamma \mu_0}{2\pi} \sqrt{H\left(H + M_{eff}\right)}$$

where f_{res} is the resonance frequency, H is the applied magnetic field, γ is the gyromagnetic ratio, and M_{eff} is the effective magnetization. The fit of the experimental data results in the effective magnetization of M_{eff} = 108.4 kA/m ($4\pi M_{eff}$ = 1362.1 Gauss). Usually, the obtained value of

M_{eff} is used to determine the uniaxial magnetocrystalline anisotropy energy density K_u following the expression

$$K_u = \frac{\mu_0 M_s}{2}\left(M_s - M_{eff}\right),$$

if the saturation magnetization M_S is known. Interpretation of the FMR data this way is complicated by the fact that the FMR measurements were conducted in the magnetic field range of approximately 0.3 – 0.6 T where, according to the magnetometry data shown in **Figure S19**, the sample is not fully saturated. As a result, the value of the saturation magnetization is between approximately 200 kA/m and the value of 253 kA/m, the latter determined in the fully saturated sample. As a result of such an ambiguity in determination of M_S, only a range of values of K_u can be determined, which we estimate to be 11.5 – 23.0 kJ/m^3, thus indicating that the magnetocrystalline anisotropy favors the out-of-plane axis. Using micromagnetic simulations we show in **Figure S16** that the uncertainty in the value of K_u does not play an important role in determining the skyrmion size and stability.

These results are consistent with the in-plane and out-of-plane SQUID loops (**Figure S19**), which show an overall preference for in-plane magnetization as indicated by the lower saturation field for the in-plane loop. While the positive K_u favors out-of-plane magnetization, the magnetic shape anisotropy $\left(\frac{1}{2}\mu_0 M_S^2\right)$ favoring in-plane magnetization is stronger, leading to an overall preference for in-plane magnetization.

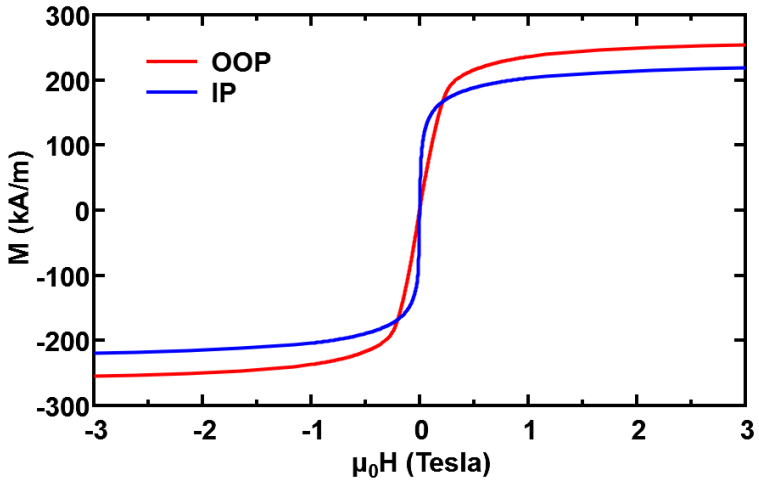

Figure S19. Out-of-plane (OOP, red) and in-plane (IP, blue) hysteresis loops of $Fe_{1.2}Ge$ obtained at 300 K.

Gilbert damping

The results of FMR measurements shown in **Figure S18c** were used to determine Gilbert damping parameter α of $Fe_{1.2}Ge$. This was extracted by fitting the frequency dependence of the linewidth ΔH with the expression:[15]

$$\Delta\mathrm{H} = \Delta H_0 + \frac{4\pi\alpha f}{\mu_0\gamma}$$

where f is the rf frequency, ΔH_0 the inhomogeneous broadening contribution to the linewidth, and γ is the gyromagnetic ratio. The fit of the frequency dependence of the linewidth results in $\alpha = 0.019$.

References

1. Ahmed, A. S., Rowland, J., Esser, B. D., Dunsiger, S. R., McComb, D. W., Randeria, M. & Kawakami, R. K. Chiral bobbers and skyrmions in epitaxial FeGe/Si(111) films. *Phys. Rev. Materials* **2,** 041401(R) (2018).

2. Bagues, N., Wang, B., Liu, T., Selcu, C., Boona, S., Kawakami, R., Randeria, M. & McComb, D. Imaging of Magnetic Textures in Polycrystalline FeGe Thin Films via in-situ Lorentz Transmission Electron Microscopy. *Microscopy and Microanalysis* **26,** 1700–1702 (2020).

3. Wang, B., Bagués, N., Liu, T., Kawakami, R. K. & McComb, D. W. Extracting weak magnetic contrast from complex background contrast in plan-view FeGe thin films. *Ultramicroscopy* **232,** 113395 (2022).

4. Gerber, A. Interpretation of experimental evidence of the topological Hall effect. *Phys. Rev. B* **98,** 214440 (2018).

5. Raju, M., Petrović, A. P., Yagil, A., Denisov, K. S., Duong, N. K., Göbel, B., Şaşıoğlu, E., Auslaender, O. M., Mertig, I., Rozhansky, I. V. & Panagopoulos, C. Colossal topological Hall effect at the transition between isolated and lattice-phase interfacial skyrmions. *Nat Commun* **12,** 2758 (2021).

6. Bruno, P., Dugaev, V. K. & Taillefumier, M. Topological Hall Effect and Berry Phase in Magnetic Nanostructures. *Phys. Rev. Lett.* **93,** 096806 (2004).

7. Verma, N., Addison, Z. & Randeria, M. Unified theory of the anomalous and topological Hall effects with phase-space Berry curvatures. *Science Advances* **8,** eabq2765 (2022).

8. Nagaosa, N. & Tokura, Y. Topological properties and dynamics of magnetic skyrmions. *Nature Nanotechnology* **8,** 899–911 (2013).

9. Banerjee, S., Rowland, J., Erten, O. & Randeria, M. Enhanced Stability of Skyrmions in Two-Dimensional Chiral Magnets with Rashba Spin-Orbit Coupling. *Phys. Rev. X* **4,** 031045 (2014).

10. Büttner, F., Lemesh, I. & Beach, G. S. D. Theory of isolated magnetic skyrmions: From fundamentals to room temperature applications. *Sci. Rep.* **8,** 4464 (2018).

11. Wang, X. S., Yuan, H. Y. & Wang, X. R. A theory on skyrmion size. *Commun. Phys.* **1,** 1–7 (2018).

12. Bera, S. & Mandal, S. S. Theory of the skyrmion, meron, antiskyrmion, and antimeron in chiral magnets. *Phys. Rev. Research* **1,** 033109 (2019).

13. Turgut, E., Paik, H., Nguyen, K., Muller, D. A., Schlom, D. G. & Fuchs, G. D. Engineering Dzyaloshinskii-Moriya interaction in B20 thin-film chiral magnets. *Phys. Rev. Materials* **2,** 074404 (2018).

14. Vansteenkiste, A., Leliaert, J., Dvornik, M., Helsen, M., Garcia-Sanchez, F. & Van Waeyenberge, B. The design and verification of MuMax3. *AIP Advances* **4,** 107133 (2014).

15. Kalarickal, S. S., Krivosik, P., Wu, M., Patton, C. E., Schneider, M. L., Kabos, P., Silva, T. J. & Nibarger, J. P. Ferromagnetic resonance linewidth in metallic thin films: Comparison of measurement methods. *Journal of Applied Physics* **99,** 093909 (2006).